HHS Public Access

Author manuscript

Curr Biol. Author manuscript; available in PMC 2022 November 08.

Published in final edited form as:

Curr Biol. 2021 November 08; 31(21): 4762–4772.e5. doi:10.1016/j.cub.2021.08.051.

Trans-inhibition of axon terminals underlies competition in the habenulo-interpeduncular pathway

Margherita Zaupa[1,6], **Seyedeh Maryam Alavi Naini**[1,6], **Maroun Abi Younes**[1], **Erika Bullier**[1], **Erik R. Duboué**[2], **Hervé Le Corronc**[1], **Hédi Soula**[3], **Sebastien Wolf**[4], **Raphael Candelier**[4], **Pascal Legendre**[1], **Marnie E. Halpern**[5], **Jean-Marie Mangin**[1], **Elim Hong**[1,*]

[1]INSERM, CNRS, Neurosciences Paris Seine - Institut de Biologie Paris Seine (NPS - IBPS), Sorbonne Université, 75005 Paris, France

[2]Jupiter Life Science Initiative, Wilkes Honors College and Charles E. Schmidt College of Science, Florida Atlantic University, Jupiter, FL USA 33458

[3]INSERM, Sorbonne Université, Nutriomics, La Pitié Salpétrière, 75013 Paris, France

[4]Laboratoire Jean Perrin, CNRS, Sorbonne Université, 75005 Paris, France

[5]Department of Molecular and Systems Biology, Geisel School of Medicine at Dartmouth, Hanover, NH USA 03755

[6]These authors contributed equally

Summary

Survival of animals is dependent on the correct selection of an appropriate behavioral response to competing external stimuli. Theoretical models have been proposed and underlying mechanisms are emerging to explain how one circuit is selected among competing neural circuits. The evolutionarily conserved forebrain to midbrain habenulo-interpeduncular nucleus (Hb-IPN) pathway consists of cholinergic and non-cholinergic neurons, which mediate different aversive behaviors. Simultaneous calcium imaging of neuronal cell bodies and of the population dynamics of their axon terminals reveals that signals in the cell bodies are not reflective of terminal activity. We find that axon terminals of cholinergic and non-cholinergic habenular neurons exhibit stereotypic patterns of spontaneous activity that are negatively correlated and localize to discrete subregions of the target IPN. Patch-clamp recordings show that calcium bursts in cholinergic terminals at the ventral IPN trigger excitatory currents in IPN neurons, which precede inhibition of non-cholinergic terminals at the adjacent dorsal IPN. Inhibition is mediated through presynaptic

*Lead Contact: elim.hong@inserm.fr.

Author Contributions

M.Z., S.W., R.C., E.R.D., P.L., M.E.H., J-M.M. and E.H. designed experiments. M.Z., E.B., M.A.Y., S.M.A.N., H.L., S.W., R.C., E.R.D., J-M.M. and E.H. conducted the experiments. M.Z., S.M.A.N., S.W., H.S., J-M.M. and E.H. analyzed data. E.H. wrote the manuscript with input from all authors.

Declaration of Interests

The authors declare no competing interests.

$GABA_B$ receptors activated in non-cholinergic habenular neurons upon GABA release from the target IPN. Together, the results reveal a hardwired mode of competition at the terminals of two excitatory neuronal populations, providing a physiological framework to explore the relationship between different aversive responses.

eToc

Zaupa et al., show that calcium signals in habenular soma are not reflective of activity in axon terminals at the interpeduncular nucleus. They uncover an atypical mode of lateral inhibition between two habenular circuits where the activation of cholinergic neurons inhibits non-cholinergic activity by retrograde signaling from their target site.

Graphical Abstract

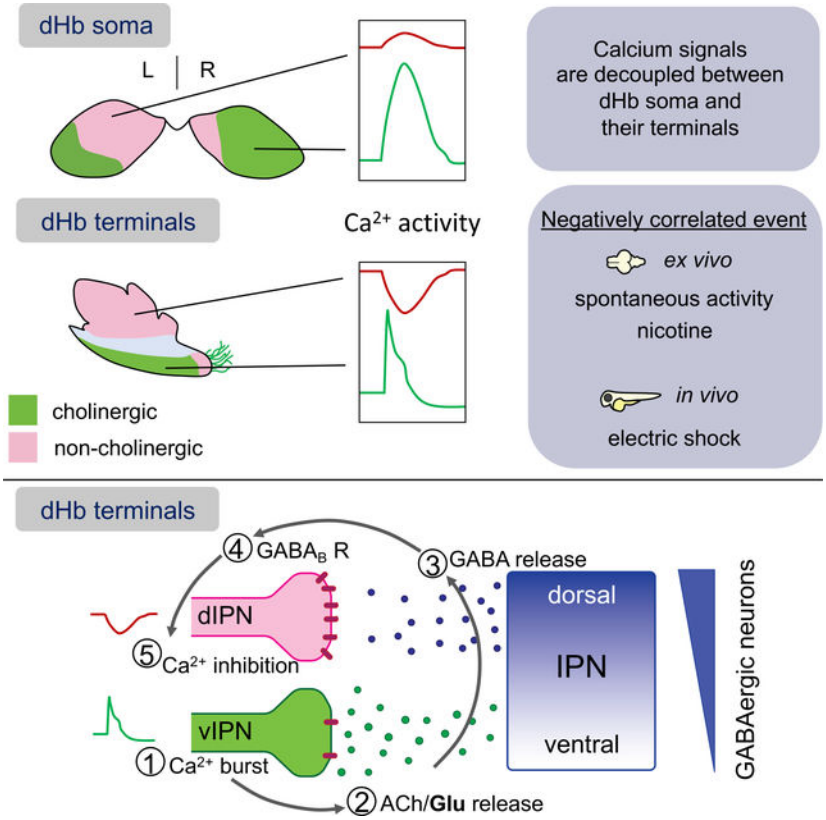

Keywords

Habenula; interpeduncular nucleus; nicotine; $GABA_B$ receptor; calcium imaging; electrophysiological recording; zebrafish

Introduction

The bilaterally paired habenular nuclei (Hb) are part of the highly conserved dorsal diencephalic conduction system connecting the limbic forebrain with monoaminergic

brainstem areas[1,2]. Anatomically, they consist of medial (MHb) and lateral (LHb) nuclei in mammals that are homologous to the dorsal (dHb) and ventral (vHb) nuclei of teleosts. The LHb/vHb send projections through the fasciculus retroflexus (FR) directly to serotonergic raphe neurons and dopaminergic neurons in the ventral tegmental area. Axons from MHb/dHb neurons course through the FR and terminate at an unpaired midbrain target, the interpeduncular nucleus (IPN). The Hb-IPN pathway is critical for understanding addiction and mood disorders due to its involvement in regulating behaviors such as stress, anxiety and fear learning[1,3–6].

The MHb/dHb contains glutamatergic neurons are divided into those that co-release acetylcholine (cholinergic) or neuropeptides, including substance P (non-cholinergic) or somatostatin[7–9]. In rodents, cholinergic and non-cholinergic neuronal populations project to central and peripheral IPN domains, respectively[7]. Gene expression analyses, fluorescent dye tracing and transgenic reporters have demonstrated left-right differences between the bilateral dHb of larval zebrafish[5,10,11]. For example, cholinergic neurons are located mainly in the right dHb and project to the ventral IPN (vIPN), whereas non-cholinergic neurons are more abundant in the left dHb and innervate the dorsal IPN (dIPN)[9,12] (Figure 1A). In rodents, cholinergic and non-cholinergic MHb neurons receive afferent input from neurons located in the triangular septum (TS) and the bed of the anterior commissure (BAC), respectively[13]. Toxin-induced ablation of TS-cholinergic or BAC-non-cholinergic MHb projections selectively impaired anxiety or fear learning behaviors[3]. Conditional genetic deletion of Cerebellin (Cbln) genes in the MHb, Cbln4 in cholinergic or Cbln2 in non-cholinergic neurons, affects freezing behavior or spatial learning, respectively[4].

The dHb responds differently to external factors such as light, odor and aversive stimuli in zebrafish larvae[6,14,15]. Inhibition of neural transmission in the non-cholinergic (dHbL) versus cholinergic (dHbM) pathways in adult zebrafish is associated with winner or loser states in a social conflict paradigm[16]. Studies in rodents and zebrafish suggest that the cholinergic and non-cholinergic MHb/dHb neuronal populations form functionally distinct, parallel circuits. However, it is unknown whether the two pathways interact or directly influence the activity of one another.

To understand functional connectivity of the dHb-IPN pathway, we took advantage of the small size of the larval zebrafish brain to monitor neural activity in whole explant preparations. Calcium imaging revealed that dHb terminals at the IPN can be resolved into distinct domains based on their signaling dynamics. We discovered an inverse relationship between cholinergic and non-cholinergic neurons only at their axon terminals. Results from pharmacology, imaging and electrophysiology experiments show that synchronized activity of cholinergic dHb neurons results in GABA release from the IPN, leading to presynaptic inhibition of non-cholinergic axon terminals. We propose a hardwired mode of competition between two neuronal populations, whereby synchronized activation of one group inhibits the activity of the other.

Results

Cholinergic and non-cholinergic dHb terminals exhibit negatively correlated calcium events

The bilateral dHb on the dorsal surface of the diencephalon form connections with the IPN deeply embedded in the ventral midbrain, making it challenging to simultaneously monitor and manipulate both pre-and post-synaptic neuronal populations. To identify the hardwired mode of action of the dHb-IPN pathway, we analyzed spontaneous activity in both regions using brain explants from larval zebrafish. The entire brain was removed from *TgBAC(gng8:GAL4ff)*^{c426}*;Tg(UAS:GCaMP7a*) larvae expressing GCaMP in dHb neuronal cell bodies and their terminals at the IPN[6]. We found that whereas most dHb neurons exhibit spontaneous activity (Video S1, Figure S1A), a large cluster of neurons on the right together with a small cluster on the left exhibited correlated calcium bursts (Figure 1B–E, Video S1). The neuronal clusters with highly correlated calcium bursts were consistently identified by *k*-means and hierarchical clustering methods (Figure 1B–E, Figure S1). Their location (Figure 1B, Figure S1, green and blue) corresponds to that previously described for cholinergic and somatostatinergic neuronal clusters in the dHb (Figure 1A)[9,12].

We examined whether similar calcium signals were present in dHb axon terminals at the IPN. As the left dHb contains cholinergic and non-cholinergic neurons, which form connections with the dorsal and ventral IPN (Figure 1A)[9,12], we carried out simultaneous calcium imaging of neurons in the left dHb and axon terminals at the IPN (Video S2). We used *k*-means clustering to identify domains in an unbiased manner since results were comparable with hierarchical clustering. Distinct domains of spontaneous activity defined stereotypic and correlated patterns of dHb neurons. The soma of the left dHb segregated into two (dorsal and ventral) and dHb axon terminals fell into three domains at the dorsal IPN (dIPN), ventral IPN (vIPN) and raphe nucleus (raphe) (Figure 1F). The activation pattern of ventral dHb soma clustered together with that of the raphe area, suggesting that these regions are functionally connected (Figure 1F, green). Surprisingly, we found that calcium signals in the dIPN were negatively correlated with those in the ventral dHb soma and raphe (Figure 1F–I, red). When an increased calcium signal (burst) occurred in the soma of the ventral dHb and terminals at the raphe, a transient decrease from baseline calcium signaling (inhibition) was observed at the dIPN (Figure 1H,I). Calcium inhibition was limited to terminals at the dIPN and was not observed in the soma of dHb neurons (Figure 1F). Indeed, analysis of different dHb focal planes in multiple explants failed to reveal neuronal cell bodies exhibiting negatively correlated calcium signals during spontaneous activity (Figure 1C–E, Figure S1). The results indicate that calcium signals in dHb soma are not always reflective of the calcium dynamics at their terminals.

Calcium signaling data also revealed a local negative interaction between dHb terminals at the IPN. We analyzed activity in dHb terminals throughout the IPN (Video S3) and by applying *k*-means clustering and manual inspection of the calcium signals, we identified five spatially segregated domains of axon terminals with distinct patterns of activity: 1) dIPN showing mainly calcium inhibition with few calcium bursts (red); 2) dorsal half of the vIPN (dvIPN) displaying frequent calcium bursts of low and high amplitude, with the

high amplitude bursts followed by calcium inhibition (grey); 3) ventral half of the vIPN (vvIPN), showing high amplitude calcium bursts followed by inhibition (blue); 4) caudal area of the vIPN (cvIPN) (magenta), which clustered together with the dIPN exhibiting calcium inhibition; and 5) raphe area exhibiting calcium bursts without inhibition (green) (Figure 1J–P).

Notably, terminals at the dIPN and raphe exhibited negatively correlated calcium signals (Figure 1L), which we refer to as negatively correlated events. Calcium inhibition only occurred in terminals at the dIPN when high amplitude bursts were observed at the vvIPN and raphe (Figure 1N) but not when calcium bursts were restricted to the dvIPN (Figure 1O). This suggests that dHb neurons that target the dvIPN differ from those innervating the vvIPN and raphe. Moreover, prior to or following a negatively correlated event, terminals at the dIPN showed higher GCaMP signals compared to those observed in the vIPN (Figure 1K,N; Figure S2A,B). The higher signals were not merely due to greater terminal density at the dIPN relative to the vIPN because we found no difference in the ratio of axon terminals in the two regions when labeled with GFP (Figure S2A'–B).

Quantification of calcium signaling kinetics revealed that the time to reach maximum amplitude (peak time) occurred earlier in terminals at the vvIPN compared to the raphe (1.13 ± 0.42 s vs. 1.59 ± 0.72 s), and the duration at half peak time (half duration) of the calcium burst was shorter (2.72 ± 0.56 s vs. 3.64 ± 1.55 s) (Figure S3A–C). Peak inhibition in terminals at the dIPN occurred later (4.33 ± 1.4 s) and lasted longer (9.2 ± 2.9 s) than the calcium bursts (Figure S3D,E). Activation at the vvIPN was followed by a period of inhibition not observed in terminals at the raphe. Therefore, to resolve the relationship between the negatively correlated events, we measured activity in terminals at the dIPN and at the raphe as a proxy for the vvIPN. We found a 931 ± 50 ms delay between the onset of the calcium burst and inhibition (Figure 2A), suggesting that calcium activity at the vvIPN triggers calcium inhibition in the dIPN.

To identify the neurotransmitter phenotype of neurons that exhibit calcium bursts at the vvIPN and raphe, we assessed Vesicular Acetylcholine Transporter (VAChT) expression by immunolabeling in *Tg(nptx2:Gal4-VP16)*^{rw0143a}*;Tg(UAS:GFP)*^{c354} larvae. We previously found that this transgenic line mainly labels non-cholinergic neurons in the left dHb and their projections to the dIPN[12]. We confirmed that GFP expression does not colocalize with VAChT protein (Figure 2B) whereas dHb terminals at the vvIPN and raphe are positive for VAChT staining in *TgBAC(gng8:GAL4ff)*^{c426}*;Tg(UAS:GFP)*^{c354} larvae (Figure 2B). We therefore conclude that calcium bursts at these regions are due to the synchronized activation of dHb cholinergic neurons (Figure 2C). Negatively correlated events are already apparent in 3-day-old larvae (Figure S4) upon emergence of spontaneous activity in dHb neurons (data not shown), suggesting that it is a hardwired mode of activity, coincident with establishment of the dHb-IPN pathway.

To determine whether external stimuli provoke negatively correlated events in vivo, we applied a mild electric shock to larvae. Indeed, we observed negatively correlated events between dHb terminals at the dIPN and vIPN/raphe (Figure 2D). However, due to tissues surrounding the brain, the resolution of calcium activity was inferior in larvae compared

with the brain explants. Nevertheless, this result indicates that negatively correlated events can be induced in vivo, suggesting it is a physiologically relevant mode of neuronal activation.

Nicotinic acetylcholine receptors do not mediate negatively correlated events

The MHb/dHb-IPN pathway shows the highest expression and greatest variety of nicotinic acetylcholine receptor (nAChR) subunits in the brain[17]. Since calcium inhibition in non-cholinergic dHb terminals is preceded by a calcium burst in cholinergic terminals, we investigated whether inhibition depends on the activation of nAChRs[9]. Perfusion of nicotine resulted in prolonged calcium inhibition of dHb terminals at the dIPN, which corresponded with an extended series of calcium bursts in dHb terminals at the raphe (Figure 3A,A', 260 ± 176 s). To determine the contribution of nAChRs in the generation of negatively correlated events, we administered mecamylamine and d-tubocurarine, effective blockers of cholinergic transmission in the larval IPN[9]. nAChRs antagonists did not attenuate, but rather increased the frequency of negatively correlated events (Figure 3B–C'). Thus, activation of nAChRs is not required for negatively correlated events between cholinergic and non-cholinergic dHb terminals at the IPN.

dHb terminal calcium bursts correlate with GABAergic currents in IPN neurons

To understand the basis for negatively correlated events, we combined calcium imaging of dHb terminals with patch-clamp recordings of neurons at the interface between the dIPN and vIPN. Recording at −60 mV (equilibrium potential of Cl^- ions) revealed that calcium bursts correlated with a barrage of postsynaptic inward currents consisting of fast and slow events (Figure 4A,B), which is due to release of glutamate and acetylcholine[9]. Recording at 0 mV (reversal potential of cationic ions) revealed that calcium bursts also correlated with a barrage of outward currents (Figure 4A',B') indicative of GABAergic inhibitory postsynaptic currents. The cholinergic/glutamatergic postsynaptic barrage was relatively short (half duration = 262 ± 124 ms) and synchronized with the onset of the calcium burst (delay = 67 ± 69 ms). In contrast, the barrage of GABAergic synaptic currents had a delayed onset (delay = 162 ± 80 ms) and lasted longer (half duration = 387 ± 143 ms). These results suggest that calcium bursts correspond to the release of glutamate and acetylcholine from dHb terminals at the IPN, which is followed by local release of GABA from IPN neurons.

Presynaptic $GABA_B$ receptors in dHb axon terminals mediate calcium inhibition

GABA has an inhibitory presynaptic action on transmitter release through metabotropic $GABA_B$ receptors[18]. We asked whether GABA released by the IPN could activate presynaptic metabotropic $GABA_B$ receptors, thereby repressing dHb terminal activity. Application of cgp55845, a $GABA_B$ receptor antagonist, resulted in a 74 ± 9 % reduction in the amplitude of calcium inhibition (−0.16 ± 0.03 vs. −0.04 ± 0.01) without affecting the amplitude of calcium bursts (0.22 ± 0.09 vs. 0.26 ± 0.13) (Figure 5A,A'). To test the role of $GABA_B$ receptors directly, we applied tetrodotoxin to inhibit the propagation of action potentials and eliminate all negatively correlated events. We then administered baclofen, a $GABA_B$ receptor agonist, and observed a prolonged decrease in the calcium baseline, similar in amplitude to that observed during inhibition of dHb terminals at the dIPN (Figure 5B,B'). Calcium imaging of dHb terminals together with patch-clamp recordings of IPN neurons

confirmed that prolonged inhibition corresponds with a decrease in the frequency of fast postsynaptic inward currents recorded in IPN neurons (Figure 5C,C').

In zebrafish, there are two $GABA_B1$ receptor genes, *$GABA_B$ receptor 1a* (*gabbr1a)* and *1b* (*gabbr1b)*[19]. We found that *gabbr1a*, but not *gabbr1b*, is prominently expressed in the dHb in a larger domain of the left nucleus compared with the right, in the location of non-cholinergic neurons (Figure 5D,E). Strikingly, *gabbr1a* transcripts localized to the dHb nuclei and were not detected in other brain regions including the IPN (Figure 5D). Together, these results suggest that calcium inhibition is due to the activation of presynaptic $GABA_B$ receptors in non-cholinergic terminals at the dIPN.

Retrograde signaling from GABAergic IPN neurons to non-cholinergic habenular inputs

To determine that inhibition of dHb terminals at the dIPN results from GABA released upon IPN activation, we carried out electrical stimulation of the IPN with calcium imaging (Figure 6A, Video S4). Activation of the IPN effectively triggered negatively correlated events consisting of the vIPN/raphe calcium burst (likely due to the activation of the dHb terminals at the vIPN) and dIPN calcium inhibition (Figure 6B). We next perfused a $GABA_B$ antagonist, cgp55845, during negatively correlated events induced by electrical stimulation and found a 90 ± 13 % decrease in calcium inhibition at the dIPN (−0.15 ± 0.07 vs. −0.02 ± 0.02) without any change in calcium bursts at the raphe (0.22 ± 0.08 vs 0.2 ± 0.06) (Figure 6B–E).

To verify the presence of GABAergic neurons in the IPN, we imaged the *TgBAC(gng8:GAL4ff)^{c426};Tg(UAS:GFP)^{c426};Tg(gad1b:|R|-GFP)* larvae in which dHb terminals are labeled with GFP and GABAergic neurons by RFP[20]. We found that nearly half of IPN neurons were labeled by gad1b:RFP (48 ± 2%, n = 3 larvae, N = 479 cells, Figure 6F), with more located in the dIPN than vIPN (79 ± 11% vs. 21 ± 11%, n = 3 larvae, N = 232 gad1b:RFP^+ cells). These results suggest that a higher concentration of GABA is released from neurons in the dIPN.

Discussion

The dHb of zebrafish larvae respond to external factors including light, odor and aversive stimuli[6,14,15]. A prerequisite to investigating the innate hardwired activity of the dHb-IPN pathway was eliminating the influence of external factors. We achieved this by performing calcium imaging using a whole brain explant preparation, in which central neural circuits including the dHb-IPN pathway remain intact. We found a stereotyped mode of spontaneous activity in dHb soma and axon terminals at the IPN.

Through pharmacological and electrophysiological manipulations, we determined that synchronized activation of dHb cholinergic neurons inhibit non-cholinergic neurons by an atypical mechanism of target-mediated, trans-inhibition at the level of axon terminals.

Negatively correlated events at axon terminals of cholinergic and non-cholinergic dHb neurons

Clustering algorithms are commonly used to segregate neurons into different functional groups during calcium imaging of neuronal soma[21–23]. The *k* value and threshold for hierarchical clustering were determined from a previous study of the zebrafish dHb[23] and manual inspection of the activity of individual neurons assigned to different clusters. We obtained similar but not identical results from *k*-means and hierarchical clustering methods. Nevertheless, the minor difference resulting from the clustering algorithms does not alter the conclusion showing that most dHb neurons on the right and a small cluster on the left show high levels of synchronized spontaneous activity. The location of these neurons corresponds to different neurotransmitter phenotypes: cholinergic and somatostatin[12], suggesting that dHb neurons expressing the same neurotransmitter function together.

In analyzing group dynamics of axon terminals, we found it important to also carry out manual inspection of raw data. For example, only calcium peaks at the vvIPN and not the dvIPN correlated with dIPN inhibition. VAChT antibody labeling in transgenic lines confirmed that cholinergic dHb terminals innervate only the vvIPN, indicating that the dvIPN is innervated by different types of neurons. In addition, a small domain in the caudal vIPN clustered together with the terminals at the dIPN. While there are currently no available molecular markers to differentiate between the dHb axon terminals at the cvIPN and dIPN, spatial segregation between the two areas suggests that they are targeted by different dHb neurons. In conclusion, cholinergic neurons exhibit synchronized activity and project to the vvIPN/raphe, which displays negatively correlated events with axon terminals at the dIPN (Figure 2C).

Nicotine promotes negatively correlated events in the dHb-IPN pathway

We found that nicotine induces prolonged duration of the negatively correlated event. We previously showed that a cocktail of nAChR antagonists inhibits approximately 80% of cholinergic currents in IPN neurons[9]. However, application of antagonists failed to attenuate but, rather, increased the frequency of negatively correlated events. The cholinergic system can increase the excitability of GABAergic interneurons in the neocortex and the lateral habenula[24,25]. Likewise, our data suggest that GABAergic neurons are activated by nAChRs in the IPN. We hypothesize that blocking nAChRs throughout the whole brain inhibits GABAergic signaling, resulting in a global increase in synchronized network activity.

While nAChR activation can generate a negatively correlated event, the release of GABA from IPN neurons to induce inhibition is predominantly triggered by glutamatergic rather than cholinergic transmission from the dHb terminals at the IPN during spontaneous activity,

Localization of the $GABA_B$ receptor to non-cholinergic terminals at the dIPN mediates presynaptic inhibition

We found that *gabbr1a* is expressed asymmetrically in a large area in the left and smaller area in the right dHb, indicating that the $GABA_B$ receptor is present in non-cholinergic neurons that innervate the dIPN in larvae. Moreover, *gad1b*-positive neurons predominate in the dIPN, suggesting that GABA released from dIPN neurons activates presynaptic

$GABA_B$ receptors on non-cholinergic terminals at the dIPN. Based on calcium imaging, pharmacology, electrical stimulation and molecular studies, we propose a model whereby 1) activation of cholinergic dHb neurons 2) activates GABAergic neurons in the IPN resulting in the 3) release of GABA that through retrograde signaling 4) activates inhibitory presynaptic $GABA_B$ receptors on non-cholinergic dHb terminals at the dIPN, leading to 5) inhibition of glutamatergic transmission (Figure 6G).

How does activation of vvIPN neurons induce GABA release by dIPN neurons? Single cell labeling experiments showed the diverse morphology of IPN neurons including those that appear to be interneurons extending their processes between the dorsal and vIPN[26]. We hypothesize that communication between vvIPN and dIPN neurons could be mediated by such interneurons connecting the dorsal and ventral IPN. Another possibility is that more vvIPN neurons are GABAergic than visualized by the transgenic line used in this study, akin to what has been shown for the adult IPN[27]. Thus, GABAergic vvIPN neurons might form direct synaptic connections, or through non-synaptic volume transmission, release GABA to inhibit non-cholinergic terminal activity at the dIPN.

As the MHb/dHb-IPN pathway is evolutionarily conserved in all vertebrates, including rodents and zebrafish[9,28], it is likely that this mode of hardwired activity is not unique to zebrafish. Indeed, a recent study on mice reports that presynaptic $GABA_B$ receptors at non-cholinergic terminals at the IPN play an inhibitory role on plasticity[29], suggesting a conserved role for these receptors.

Model for competitive selection between dHb circuits on behavior

It is crucial for an animal to identify the most salient stimulus amongst many concurrent external stimuli and select a single behavioral response. One example is the flight, freeze or fight response[30]. During early stages of development, hardwired circuits to execute specific behavioral repertoires, such as escape (flight), are essential for survival[31]. The process of transforming multiple sensory inputs into a single behavioral outcome is termed competitive selection and includes selective attention and decision-making [32]. Computational formulations such as winner-take-all models have been proposed[33,34] and recent studies have begun to elucidate the mechanisms for behavioral selection in competing circuits[35–38].

Higher baseline GCaMP fluorescence in the terminals at the dIPN relative to the vIPN suggests that non-cholinergic neurons display high frequency oscillation[39]. We propose that the synchronized burst in cholinergic terminals at the vIPN transiently inhibits this constitutive activity that occur in non-cholinergic neurons, ensuring only one pathway is active at any given time.

What could be the advantage of having local inhibition at the terminal level? Different external stimuli preferentially activate left or right dHb neurons[6,14,15]. However, the ratio of asymmetric dHb activation depends on the intensity of the stimulus for both light and electric shock (personal observations), suggesting that the left and right dHb can be co-activated by the same stimulus. We suspect that this setup of local inhibition would

ensure that 1) only one circuit is active at a time and 2) upon exposure to multiple stimuli a hierarchy is established between the stimuli.

Aversive behavior refers to emotional states with negative valence, such as fear or anxiety. Fear is defined as a response to a factual known threat while anxiety to an unknown, poorly defined threat. Brain areas that contribute to fear and anxiety exhibit great overlap including the amygdala, medial prefrontal cortex and the hippocampus[40]. While recent optogenetic and in vivo studies have begun unraveling the microcircuits that participate in these behaviors[35,41], how they interact with other areas of the brain are unclear. The highly conserved MHb/dHb-IPN pathway–consists of two circuits composed of different neuronal populations, which mediate fear- or anxiety-related behaviors[3–5,16]. We propose that the trans-inhibition mechanism between cholinergic and non-cholinergic dHb-IPN circuits underlies competitive selection of aversive behavioral responses.

A brief electric shock induces fast swim followed by freezing behavior before returning to baseline locomotion in larval zebrafish[6]. Here, we demonstrate that it can also promote negatively correlated events in the dHb terminals at the IPN. We hypothesize that activation of the cholinergic pathway by electric shock results in a stereotypical fast swim (flight) response, which is followed by inhibition of the non-cholinergic pathway allowing the animal to freeze. Prior to puberty, a flight/freeze response would be more beneficial than a fight response. In juveniles/adults, this dual circuit likely becomes more complex as different neuropeptides become expressed in the dHb-IPN pathway and with the maturation of behavioral repertoires from prior experience. For example, adult zebrafish exhibit a fight or flight response, manifested by a “winner” or “loser” phenotype in a social conflict paradigm, which is correlated with potentiation in non-cholinergic and cholinergic neuronal terminals, respectively[16]. We hypothesize that the “loser”/flight behavior corresponds to the default response to an aversive stimulus upon activation of the cholinergic pathway. The “winner”/fight behavior could result from preferential hyper-activation of the non-cholinergic pathway, corresponding to a heightened level of anxiety.

In conclusion, investigating neuronal population dynamics within an intact pathway has revealed an atypical mode of trans-inhibition between two excitatory neuronal populations at their axon terminals. This hardwired mode of competition could underlie the mechanism for competitive selection between these neural circuits and provide a physiological framework to explore the relationship between anxiety and fear.

STAR Methods

RESOURCE AVAILABILITY

Lead contact—Further information and requests for resources and reagents should be directed to and will be fulfilled by the Lead Contact, Elim Hong (elim.hong@inserm.fr).

Material availability—All plasmids generated in this study are available upon request to the Lead Contact.

Data and code availability

- All data reported in this paper will be shared by the Lead Contact upon request.
- This paper does not report original code.
- Any additional information required to reanalyze the data reported in this paper is available from the Lead Contact upon request.

EXPERIMENTAL MODEL AND SUBJECT DETAILS

AB wild-type and transgenic zebrafish lines *TgBAC(gng8:GAL4ff)*^{c426}, *Tg(UAS:GCaMP7a), Tg(nptx2:Gal4-VP16)*^{rw0143a}, *Tg(gad1b:|R|-GFP), Tg(UAS:GFP)*^{c354}[5,9,20,42,43] were used. Fish were maintained at 28°C on a 14:10h light: dark cycle in a recirculating system. All experiments were carried out in agreement with the European Directive 210/63/EU on the protection of animals used for scientific purposes and the French application decree ‘Décret 2013–118’. The projects of our research group have been approved by the ethical committee ‘Comité d’éthique Charles Darwin’ (APAFIS#15909–2018070912072530 v5). The fish facility has been approved by the French ‘Service for animal protection and health’ (A-75–05-25).

METHOD DETAILS

Explant Dissection—*TgBAC(gng8:GAL4ff)*^{c426}*;Tg(UAS:GCaMP7a*) 3, 6 and 7 day-post-fertilization (dpf) larvae were used for experiments. Larvae were anesthetized in Tricaine (0.01%) and brains dissected using fine forceps in ice cold Ringer’s solution (134mM NaCl, 2.1 KCl, 1.2mM $MgCl_2$, 10 mM HEPES, 10mM Glucose, 2.1 $CaCl_2$, pH = 7.6) and mounted in 1.2% low melting agarose for calcium imaging and electrophysiology experiments.

Pharmacology—Drugs were applied to the explants either directly using a pipette or by using a perfusion peristaltic pump (Ismatec) at a rate of 5–6 ml/min. Mecamylamine hydrochloride (100 μM), (+)-D-tubocurarine chloride (10 μM), nicotine ditartrate (10 μM, Acros Organics), tetrodotoxin (3 μM), baclofen (2 μM) and cgp55845 (1 μM) were used. The drugs were purchased from Tocris Bioscience unless otherwise noted.

Calcium Imaging—Calcium imaging was performed on a spinning disk microscope (Zeiss Axio Examiner.Z1) using a 40X water immersion objective (NA =0.95) or Leica SP5 laser scanning confocal microscope using a 25X water immersion objective (NA = 0.95). Images were acquired at a rate between 2.2–6.7Hz, depending on the experiment. Nicotine was perfused for 5 minutes followed by E3 medium to wash out the drug. For experiments with mecamylamine hydrochloride and D-tubocurarine chloride, as a short-term application did not show any changes in calcium signals, we carried out the following experiment to assay for long-term change: baseline calcium signals were recorded for 15 minutes before pipetting the drug directly to the explant. The calcium signals were recorded for an additional 45 minutes after drug application. For the cgp55845 and baclofen experiments, 10–15 minutes baseline activity was recorded followed by drug application using the perfusion system and imaged for another 15 minutes.

Patch-clamp recordings and simultaneous Ca^{2+} imaging—Explants from *TgBAC(gng8:GAL4ff)*^{c426}*;Tg(UAS:GCaMP7a*) larvae were placed in a recording chamber and constantly perfused with Ringer's solution at a rate of 1–2 mL/min. The IPN was made accessible for patch-clamp recordings and Ca^{2+} imaging by orienting the explants with the ventral surface upward. dHb terminals and the IPN were located and imaged using a 63x water immersion objective mounted on an epifluorescence microscope BX51W1 (Olympus) equipped with a 470 nm LED fluorescent excitation light. Patch electrodes were filled with an intracellular solution containing 130 mM CsMeSO4, 4 mM MgCl2, 4 mM Na-ATP, 0.3 mM Na-GTP, 10 mM Hepes, and 10 mM EGTA, 5 mM QX-314 adjusted to pH 7.2, 290 mOsm, for resistances between 5 and 8 MΩ. This intracellular solution allowed discrimination of cationic excitatory currents and chloride inhibitory currents based on their distinct reversal potentials (E_{cation} = 0 mV; E_{Cl} = −60 mV). By recording the cells at −60 mV, EPSCs appeared as inward currents, whereas IPSCs were barely detectable. Conversely, IPSCs appeared as outward currents when recording the cells at a holding potential of −0 mV, while EPSCs became undetectable. Whole-cell recordings were obtained using a Multiclamp 700B amplifier connected to a digidata 1440 acquistion system monitored using pClamp 10 software (Molecular Devices). Analyses were performed using Clampfit 10 (Molecular Devices). For all experiments, data were filtered at 4 kHz during recording and the traces were digitized at 20 kHz.

Simultaneous time-lapse imaging of GCaMP fluorescence in dHb terminals was performed using either an Orca Flash4.0 (Hamamatsu, Japan) or Orca 03G (Hamamatsu, Japan) camera and recorded using the HC Image Live software (Hamamatsu, Japan) at an acquisition frequency of 5 Hz or 10Hz with an exposure time of 200 ms and 100 ms, respectively. Time-lapse and patch-clamp acquisition were synchronized via a TTL signal sent to the camera via the pClamp 10 software. Time-lapse frames were encoded at a 256×256 pixel resolution using a 16-bit grey scale. Time-lapse images were analyzed using the ImageJ software (National Institute of Health, USA) and fluorescence signals were plotted using Clampfit 10.

Immunohistochemistry—*TgBAC(gng8:GAL4ff)*^{c426}*;Tg(UAS:GFP)*^{c354} 6 dpf larvae were fixed in BT fix (4% PFA, 0.15mM $CaCl_2$, 4% sucrose in 1x PBS) overnight in 4°C for rabbit anti-VAChT (1/200, Synaptic systems) labeling. Larvae were embedded in 4% low melt agarose and sectioned to 50μm using a vibratome (Leica, Inc). Floating sections were incubated in primary antibody in incubating solution (0.8% Triton-X in 1x PBS) for 3 days on a shaker in 4°C. The sections were washed and incubated in secondary anti-rabbit Alexa Fluor 594 (1:1000) with Hoechst 33342 (1:2000) overnight at 4°C on a shaker. *TgBAC(gng8:GAL4ff)*^{c426}*;Tg(UAS:GFP* ^{c354}*;Tg(gad1b:|R|-GFP)* larvae were fixed overnight in 4% PFA, sectioned to 50μm and incubated with Hoechst 33342 (1:2000) overnight at 4°C on a shaker. All sections were then mounted on slides using Mowiol (Sigma). They were imaged using the Leica TCS SP5 AOBS upright microscope using a 63x (N.A. = 1.4) objective.

RNA in situ Hybridization—PCR fragments for *gabbr1a* (ENSDARG00000018967) (553-bp) and *gabbr1b* (ENSDARG00000016667) (539-bp) were subcloned into

pCRII-TOPO vector using the TOPO®TA cloning Kit (Invitrogen). Reverse primer sequences were from [19]. The following forward primers were used: ***gabbr1a*** (ACGTATGGTTCCTCATCGGC) ***gabbr1b*** (AGACAAGAGAAAGCACCTGGA). Restriction enzymes and RNA polymerase used to synthesize the antisense RNA probes are as follows: *gabbr1a* (*KpnI*/T7), *gabbr1b* (*KpnI*/T7). Colorimetric in situ hybridization (ISH) assay was performed as described in[45]. Following ISH, the larvae were mounted in 100% glycerol and imaged on a Nikon Eclipse E800 microscope.

Electrical shock assay—Custom built electrical stimuli setup consisted of copper mesh electrodes that were mounted 6 cm apart on opposing sides and connected to a DS3 isolated constant current stimulator (Digitimer, Ltd.). Three electrical field stimulations (6mA, 20V, 500msec) were triggered every five minutes by MetaMorph (Molecular Devices). The larvae were paralyzed in 2% pancuranium bromide and mounted in the middle of 90mm diameter petri dishes filled with 30 ml E3 medium to ensure consistent stimulation. Shock assay was performed in 6–7 dpf agarose-restricted larvae, paralyzed with 2% pancuranium bromide.

Electrical stimulation—The IPN neurons were stimulated using a low-resistance (<1MΩ) glass pipette filled with Ringer solution containing an AgCl electrode. Train stimulations (20μs duration 50Hz stimulations lasting 400ms) were triggered every 1 minute with an isolated current stimulator (DS3; Digitimer Ltd.) using a Master-8 pulse generator (A.M.P.I). Prior to each experiment, a dose-dependent curve was performed to select the optimal setting that induced negatively correlated events in the terminals at the IPN. Stimuli ranged between 100 μA – 1.2 mA.

QUANTIFICATION AND STATISTICAL ANALYSIS

Calcium data analysis—Average fluorescence intensity of habenular soma was calculated by manually drawing regions of interest (ROI) in FIJI as described in[6]. To carry out a non-biased analysis of the dHb-IPN pathway and dHb terminals at the IPN, 2×2 μm^2 grid ROIs were drawn over the entire recording using FIJI macro. Average fluorescence intensity for each ROI was then extracted per frame and analyzed on MATLAB using custom written scripts.

Amplitude of calcium signal was calculated according to the formula:

$$\Delta F/F = (F_i - F_{mean})/F_{mean},$$

whereby, F_i is the mean intensity in a single ROI at a single time point while F_{mean} is the mean intensity in a single ROI throughout the entire recording time. Multiple clustering algorithms were tested including functional clustering algorithm [44] and spectral clustering on calcium traces and correlation coefficient values. After comparing the clusters generated using various algorithms, we found *k*-means and hierarchical clustering based on pairwise linear correlation matrix were the most representative of calcium signals in the spontaneous activity recordings. K-means and hierarchical clustering based on pairwise linear correlation matrix were carried out on MATLAB using *kmeans* and *linkage* functions (‘euclidean’ distance and ‘complete’ method), respectively. Different k values were tested and k = 5 was

selected based on manual inspection of calcium signals in the time-lapse recordings and also using a heatmap. The correlation matrix displayed in figures was generated by calculating the correlation coefficients between the average calcium signal traces for each cluster.

The threshold for hierarchical clustering was determined by manual inspection of the calcium signals in the recording and heatmap. Once specific IPN domains were identified by *k*-means, larger ROIs were manually drawn containing the different IPN domains. Analysis of calcium burst frequency using 'findpeaks' function was performed in MATLAB (Mathworks). Peak of calcium burst, calcium inhibition and half duration were identified using *findpeaks* and *half prominence* functions in MATLAB and verified manually. Calcium burst peak was defined by the highest value during a calcium burst. Peak of calcium inhibition was defined by the lowest value during a calcium inhibition event. Half duration was calculated as the width of the calcium signal at the half value of a peak during a calcium burst or inhibition. All graphs and plots were made on MATLAB using custom written scripts.

Statistical analysis—Statistical tests were carried out using a Wilcoxon signed rank test for averaged paired samples, Kruskal-Wallis test followed by a Dunn's test for comparison between more than 2 groups, Mann-Whitney test was used with independent samples and a linear mixed model with fixed effect was used to compare multiple values from repeated events. All statistical tests were performed on R or GraphPad Prism (GraphPad Software, Inc.). $p < 0.05$ was considered as statistically significant. All statistical details including statistical tests, exact values of n, value representation (mean ± SD) are indicated in the figure legends.

Supplementary Material

Refer to Web version on PubMed Central for supplementary material.

Acknowledgements

We thank Hitoshi Okamoto for insightful feedback on this project; Marco Diana and Nathalie Leresche for advice on pharmacology experiments; Eric Schwartz and Soumaiya Imarraine for helpful comments on the manuscript; Jean-Pierre Coutanceau for aid in zebrafish husbandry; and the IBPS aquatic animal facility and imaging facility. Hitoshi Okamoto, Koichi Kawakami and Shin-ichi Higashijima provided the *Tg(nptx2:Gal4-VP16)*^{rw0143a}, *Tg(UAS:GCaMP7a)* and *Tg(gad1b:LOXP-DsRed-LOXP-GFP)* lines. This study was supported by a graduate fellowship from the Alexis and Anne Marie Habib Foundation (to M.A.Y), NIH grant R37HD091280 (to M.E.H.) and the ATIP-Avenir young investigator grant (INSERM/CNRS) and Emergence grant (Sorbonne Université) (to E.H).

References

1. McLaughlin I, Dani JA, and De Biasi M (2017). The medial habenula and interpeduncular nucleus circuitry is critical in addiction, anxiety, and mood regulation. J. Neurochem. 142, 130–143. [PubMed: 28791703]
2. Fakhoury M (2018). The dorsal diencephalic conduction system in reward processing: Spotlight on the anatomy and functions of the habenular complex. Behav. Brain Res. 348, 115–126. [PubMed: 29684476]
3. Yamaguchi T, Danjo T, Pastan I, Hikida T, and Nakanishi S (2013). Distinct roles of segregated transmission of the septo-habenular pathway in anxiety and fear. Neuron 78, 537–544. [PubMed: 23602500]

4. Seigneur E, Polepalli JS, and Südhof TC (2018). Cbln2 and Cbln4 are expressed in distinct medial habenula-interpeduncular projections and contribute to different behavioral outputs. Proc. Natl. Acad. Sci. U. S. A. 115, E10235–E10244. [PubMed: 30287486]
5. Agetsuma M, Aizawa H, Aoki T, Nakayama R, Takahoko M, Goto M, Sassa T, Amo R, Shiraki T, Kawakami K, et al. (2010). The habenula is crucial for experience-dependent modification of fear responses in zebrafish. Nat Neurosci 13, 1354–1356. [PubMed: 20935642]
6. Duboué ER, Hong E, Eldred KC, and Halpern ME (2017). Left Habenular Activity Attenuates Fear Responses in Larval Zebrafish. Curr. Biol. 27, 2154–2162.e3. [PubMed: 28712566]
7. Cuello AC, Emson PC, Paxinos G, and Jessell T (1978). Substance P containing and cholinergic projections from the habenula. Brain Res. 149, 413–429. [PubMed: 352479]
8. Kadar T, Silbermann M, Steinhagen-Thiessen E, and Levy A (1989). Age-related changes in the cholinergic components within the central nervous system of cw1 female mice. I. Structural analysis. Mech. Ageing Dev. 47, 133–144. [PubMed: 2716365]
9. Hong E, Santhakumar K, Akitake C. a, Ahn SJ, Thisse C, Thisse B, Wyart C, Mangin J-M, and Halpern ME (2013). Cholinergic left-right asymmetry in the habenulo-interpeduncular pathway. Proc. Natl. Acad. Sci. U. S. A. 110, 21171–6. [PubMed: 24327734]
10. Aizawa H, Bianco IH, Hamaoka T, Miyashita T, Uemura O, Concha ML, Russell C, Wilson SW, and Okamoto H (2005). Laterotopic representation of left-right information onto the dorso-ventral axis of a zebrafish midbrain target nucleus. Curr. Biol. 15, 238–243. [PubMed: 15694307]
11. Gamse JT, Kuan YS, Macurak M, Brosamle C, Thisse B, Thisse C, and Halpern ME (2005). Directional asymmetry of the zebrafish epithalamus guides dorsoventral innervation of the midbrain target. Development 132, 4869–4881. [PubMed: 16207761]
12. deCarvalho TN, Subedi A, Rock J, Harfe BD, Thisse C, Thisse B, Halpern ME, and Hong E (2014). Neurtransmitter map of the asymmetric dorsal habenular nuclei of Zebrafish. Genesis 52, 636–655. [PubMed: 24753112]
13. Otsu Y, Lecca S, Pietrajtis K, Rousseau CV, Marcaggi P, Dugué GP, Mailhes-Hamon C, Mameli M, and Diana MA (2018). Functional Principles of Posterior Septal Inputs to the Medial Habenula. Cell Rep. 22, 693–705. [PubMed: 29346767]
14. Zhang B, Yao Y, Zhang H, Kawakami K, and Du J (2017). Left Habenula Mediates Light-Preference Behavior in Zebrafish via an Asymmetrical Visual Pathway. Neuron 93, 914–928.e4. [PubMed: 28190643]
15. Dreosti E, Vendrell Llopis N, Carl M, Yaksi E, and Wilson SW (2014). Left-right asymmetry is required for the habenulae to respond to both visual and olfactory stimuli. Curr. Biol. 24, 440–445. [PubMed: 24508167]
16. Chou MY, Amo R, Kinoshita M, Cherng BW, Shimazaki H, Agetsuma M, Shiraki T, Aoki T, Takahoko M, Yamazaki M, et al. (2016). Social conflict resolution regulated by two dorsal habenular subregions in zebrafish. Science (80-.). 352, 87–90.
17. Antolin-Fontes B, Ables JL, Görlich A, and Ibañez-Tallon I (2015). The habenulo-interpeduncular pathway in nicotine aversion and withdrawal. Neuropharmacology 96, 213–222. [PubMed: 25476971]
18. Dutar P, and Nicoll RA (1988). A physiological role for GABAB receptors in the central nervous system. Nature 332, 156–8. [PubMed: 2831457]
19. Cocco A, Rönnberg AMC, Jin Z, André GI, Vossen LE, Bhandage AK, Thörnqvist P-O, Birnir B, and Winberg S (2017). Characterization of the γ-aminobutyric acid signaling system in the zebrafish (Danio rerio Hamilton) central nervous system by reverse transcription-quantitative polymerase chain reaction. Neuroscience 343, 300–321. [PubMed: 27453477]
20. Satou C, Kimura Y, Hirata H, Suster ML, Kawakami K, and Higashijima S (2013). Transgenic tools to characterize neuronal properties of discrete populations of zebrafish neurons. Development 140, 3927–31. [PubMed: 23946442]
21. Panier T, Romano SA, Olive R, Pietri T, Sumbre G, Candelier R, and Debrégeas G (2013). Fast functional imaging of multiple brain regions in intact zebrafish larvae using selective plane illumination microscopy. Front. Neural Circuits 7, 65. [PubMed: 23576959]

22. Dunn TTW, Mu YY, Narayan S, Randlett O, Naumann EEA, Yang CC-T, Schier AFA, Freeman J, Engert F, Ahrens MBMB, et al. (2016). Brain-wide mapping of neural activity controlling zebrafish exploratory locomotion. Elife 5, e12741. [PubMed: 27003593]
23. Jetti SK, Vendrell-Llopis N, and Yaksi E (2014). Spontaneous activity governs olfactory representations in spatially organized habenular microcircuits. Curr. Biol. 24, 434–439. [PubMed: 24508164]
24. Picciotto MR, Higley MJ, and Mineur YS (2012). Acetylcholine as a Neuromodulator: Cholinergic Signaling Shapes Nervous System Function and Behavior. Neuron 76, 116–129. [PubMed: 23040810]
25. Jo YH, and Role LW (2002). Cholinergic modulation of purinergic and GABAergic co-transmission at in vitro hypothalamic synapses. J. Neurophysiol. 88, 2501–2508. [PubMed: 12424289]
26. Bianco IH, Carl M, Russell C, Clarke JDW, and Wilson SW (2008). Brain asymmetry is encoded at the level of axon terminal morphology. Neural Dev. 3, 1–20.
27. Mueller T, and Guo S (2009). The distribution of GAD67-mRNA in the adult zebrafish (teleost) forebrain reveals a prosomeric pattern and suggests previously unidentified homologies to tetrapods. J. Comp. Neurol. 516, 553. [PubMed: 19673006]
28. Ren J, Qin C, Hu F, Tan J, Qiu L, Zhao S, Feng G, and Luo M (2011). Habenula " Cholinergic" Neurons Corelease Glutamate and Acetylcholine and Activate Postsynaptic Neurons via Distinct Transmission Modes. Neuron 69, 445–452. [PubMed: 21315256]
29. Melani R, Von Itter R, Jing D, Koppensteiner P, and Ninan I (2019). Opposing effects of an atypical glycinergic and substance P transmission on interpeduncular nucleus plasticity. Neuropsychopharmacology 44, 1828–1836. [PubMed: 31005058]
30. Eilam D (2005). Die hard: A blend of freezing and fleeing as a dynamic defense - Implications for the control of defensive behavior. In Neuroscience and Biobehavioral Reviews (Pergamon), pp. 1181–1191.
31. Hale ME, Katz HR, Peek MY, and Fremont RT (2016). Neural circuits that drive startle behavior, with a focus on the Mauthner cells and spiral fiber neurons of fishes. J. Neurogenet. 30, 89–100. [PubMed: 27302612]
32. Mysore SP, and Kothari NB (2020). Mechanisms of competitive selection: A canonical neural circuit framework. Elife 9.
33. Yuille AL, and Grzywacz NM (1989). A Winner-Take-All Mechanism Based on Presynaptic Inhibition Feedback. Neural Comput. 1, 334–347.
34. Maass W (2000). On the computational power of winner-take-all. Neural Comput. 12, 2519–2535. [PubMed: 11110125]
35. Fadok JP, Krabbe S, Markovic M, Courtin J, Xu C, Massi L, Botta P, Bylund K, Müller C, Kovacevic A, et al. (2017). A competitive inhibitory circuit for selection of active and passive fear responses. Nature 542, 96–99. [PubMed: 28117439]
36. Shang C, Chen Z, Liu A, Li Y, Zhang J, Qu B, Yan F, Zhang Y, Liu W, Liu Z, et al. (2018). Divergent midbrain circuits orchestrate escape and freezing responses to looming stimuli in mice. Nat. Commun. 9, 1–17. [PubMed: 29317637]
37. Hong W, Kim DW, and Anderson DJ (2014). Antagonistic control of social versus repetitive self-grooming behaviors by separable amygdala neuronal subsets. Cell 158, 1348–1361. [PubMed: 25215491]
38. Koyama M, Minale F, Shum J, Nishimura N, Schaffer CB, and Fetcho JR (2016). A circuit motif in the zebrafish hindbrain for a two alternative behavioral choice to turn left or right. Elife 5.
39. Li P, Geng X, Jiang H, Caccavano A, Vicini S, and Wu JY (2019). Measuring sharp waves and oscillatory population activity with the genetically encoded calcium indicator GCaMP6f. Front. Cell. Neurosci. 13, 274. [PubMed: 31275115]
40. Tovote P, Fadok JP, and Lüthi A (2015). Neuronal circuits for fear and anxiety. Nat. Rev. Neurosci. 16, 317–331. [PubMed: 25991441]
41. Tovote P, Esposito MS, Botta P, Chaudun F, Fadok JP, Markovic M, Wolff SBE, Ramakrishnan C, Fenno L, Deisseroth K, et al. (2016). Midbrain circuits for defensive behaviour. Nature 534, 206. [PubMed: 27279213]

42. Muto A, Ohkura M, Kotani T, Higashijima S, Nakai J, and Kawakami K (2011). Genetic visualization with an improved GCaMP calcium indicator reveals spatiotemporal activation of the spinal motor neurons in zebrafish. Proc Natl Acad Sci U S A 108, 5425–5430. [PubMed: 21383146]

43. Akitake CM, Macurak M, Halpern ME, and Goll MG (2011). Transgenerational analysis of transcriptional silencing in zebrafish. Dev. Biol. 352, 191–201. [PubMed: 21223961]

44. Feldt S, Waddell J, Hetrick VL, Berke JD, and Zochowski M (2009). Functional clustering algorithm for the analysis of dynamic network data. Phys. Rev. E - Stat. Nonlinear, Soft Matter Phys. 79.

45. Thisse B, and Thisse C (2014). In situ hybridization on whole-mount zebrafish embryos and young larvae. Methods Mol. Biol. 1211, 53–67. [PubMed: 25218376]

Highlights

- Calcium signals in habenular (Hb) soma do not reflect axon terminal activity
- Synchronized Hb cholinergic activity inhibits non-cholinergic terminals
- Presynaptic inhibition of non-cholinergic terminals is mediated by $GABA_B$ receptors
- $GABA_B$ R activation by retrograde signaling from the interpeduncular nucleus

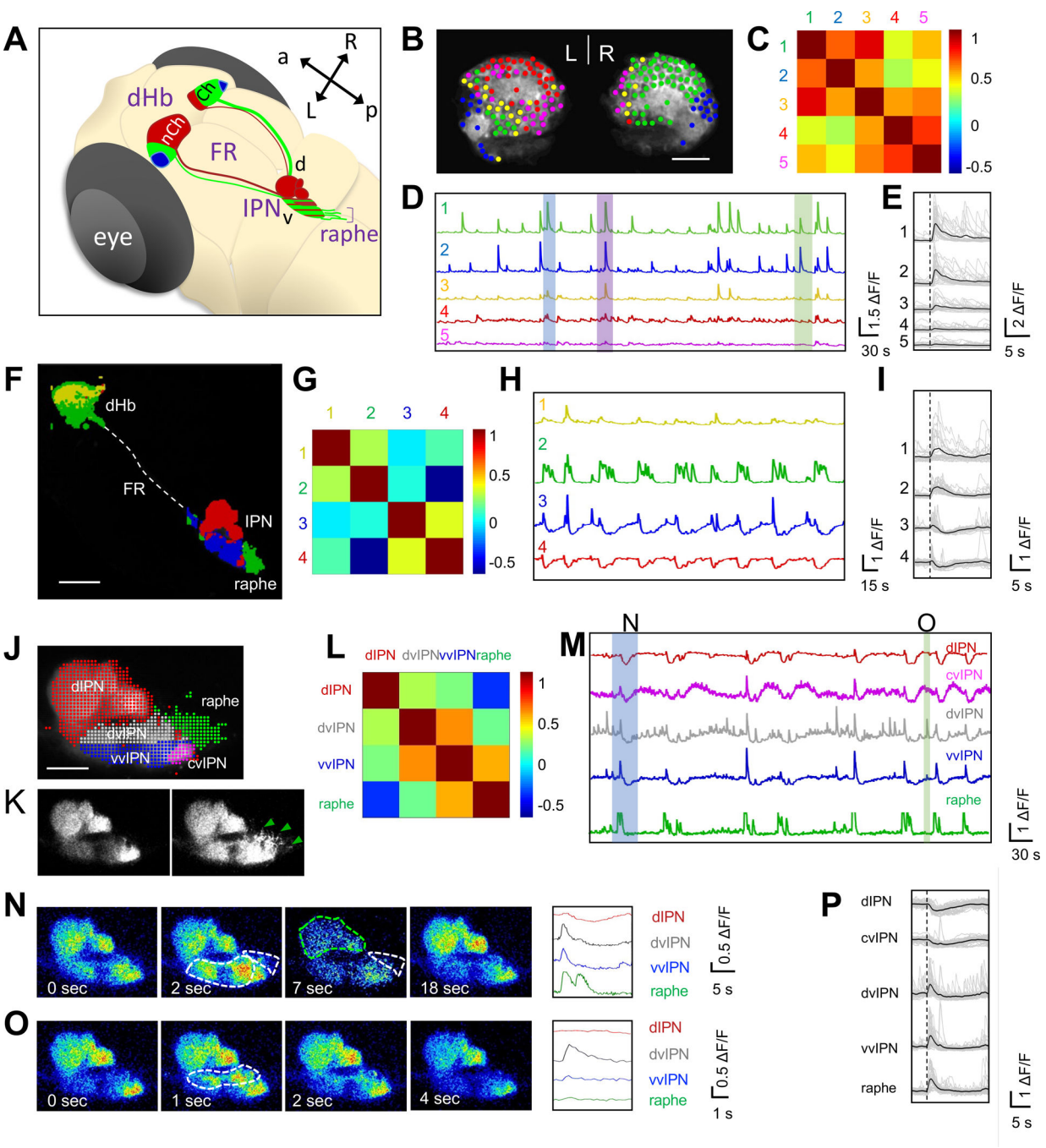

Figure 1. Identification of functional domains in dHb-IPN pathway during spontaneous activity

(A) Schematic of dHb-IPN pathway of larval zebrafish. Non-cholinergic (nCh, red) neurons are mainly in the left dHb and project to the dorsal IPN (d) whereas cholinergic (Ch, green) neurons are largely in the right dHb and project to the ventral IPN (v) and raphe (bracket). Somatostatinergic neurons are depicted in blue. Anterior (a), posterior (p), left (L) and right (R).

(B, F, J) Representative 6 day post fertilization (dpf) *Tg(gng8:GAL4ff)*^{c426}*;Tg(UAS:GCaMP7a)* brain explants expressing GCaMP in dHb

neurons (B), left dHb and their terminals (F) and terminals at the IPN and raphe (J), overlaid by colored circles representing functional domains identified by *k*-means clustering. Dotted line depicts the fasciculus retroflexus (FR) in (F).

(C, G, L) Correlation matrix of average ΔF/F signals between different clusters of dHb soma (C), dHb soma and terminals (G) and terminals at the IPN and raphe (L).

(D, H, M) Average ΔF/F traces from each cluster in 10-minute recordings. Colored boxed events in (D) correspond to single frame images in Figure S1.

(E, I, P) Average ΔF/F traces (black) of individual calcium events (grey).

(E) Traces of green/blue neurons exhibiting synchronized activity. n = 6 explants, 29 events. See Video S1.

(I) Traces of calcium bursts in the ventral dHb and dHb terminals at the vIPN and raphe (green, blue). Note that dHb terminals at the dIPN exhibit inhibition (trace 4). n = 5 explants, 24 events. See Video S2.

(P) Traces of negatively correlated events in dHb terminals at the IPN and raphe. n = 6 explants, 35 calcium events. See Video S3.

(K) Lateral view of dHb terminals expressing GCaMP7a at the IPN and raphe (green arrowheads) before and during a calcium burst event.

(N,O) Single frame images showing calcium signal changes. Blue (N) and green (O) boxed events in (M) are shown. Areas with increased (white) or decreased (green) signals are outlined (dotted lines). Right panels show traces in the IPN and raphe during the calcium event on left. n = 21/23 explants show similar calcium signaling domains.. Scale bars: 20 μm (B,J) or 50 μm (F). See also Figures S1–S4.

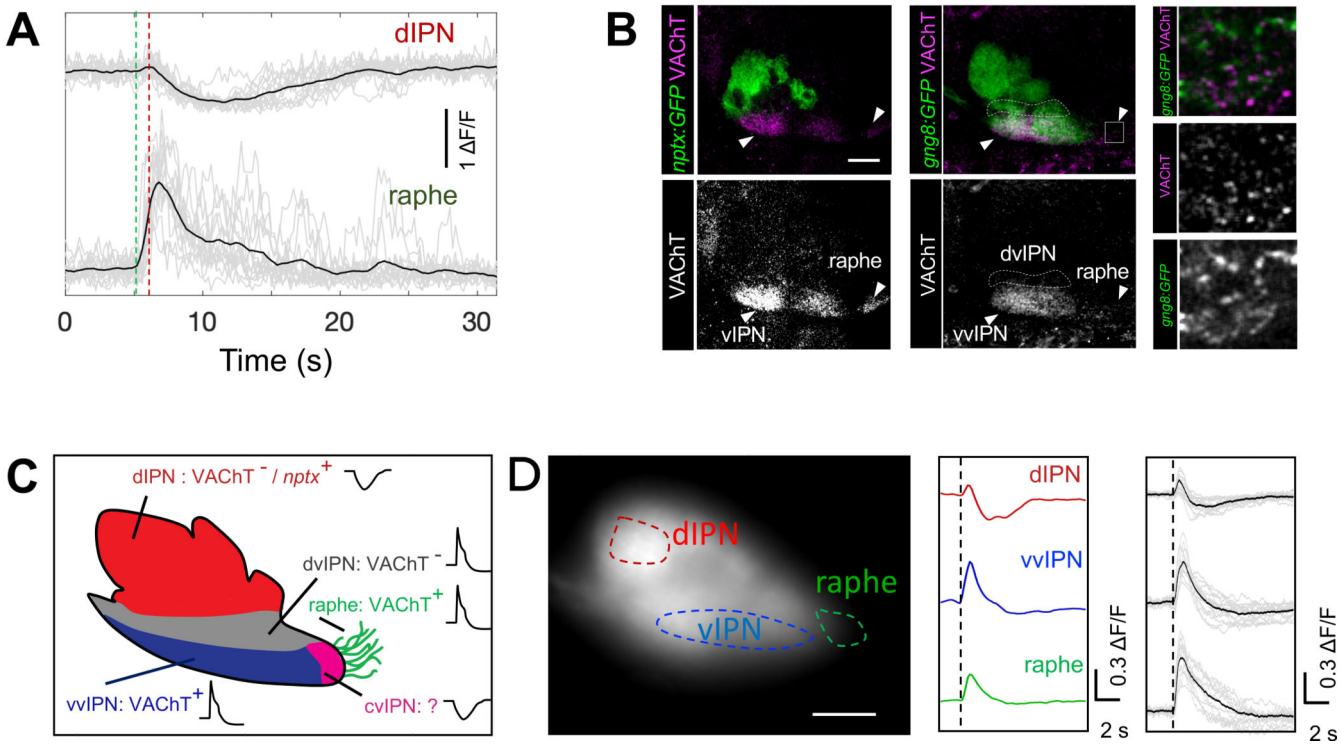

Figure 2. Synchronized cholinergic terminal activity at vIPN/raphe precedes non-cholinergic terminal inhibition at dIPN

(A) Average ΔF/F trace (black) of negatively correlated events (grey) in dHb terminals at the dIPN (top) and raphe (bottom). Time of increase (green) and inhibition (red) are indicated (dotted lines). Note the delay between the two events (931 ± 50 ms, n= 5 explants, 62 events).

(B) Sagittal sections of anti-GFP (green) and anti-VAChT (magenta) labeling in 6 dpf *Tg(nptx2:Gal4-VP16)*^{rw0143a}*;Tg(UAS:GFP)*^{c426} (left) and *Tg(gng8:GAL4ff)*^{c426}*;Tg(UAS:GFP)*^{c426} (middle) larvae. White arrowheads indicate VAChT labeling in vvIPN and raphe. White box (middle) corresponds to magnified panels on right. Scale bar: 20 μm.

(C) Summary of dHb terminal domains. nptx:Gal4;UAS:GFP-positive dIPN domain is indicated (nptx^{+}). The cvIPN is only identified based on calcium signals. Calcium bursts (green) and inhibition (red) are labeled with graph plots.

(D) Electric shock induces negatively correlated events. Left: Lateral view of *Tg(gng8:GAL4ff)*^{c426}*;Tg(UAS:GCaMP7a)* larva expressing GCaMP in dHb terminals. dIPN, vIPN and raphe are outlined (dotted lines). Middle: Representative ΔF/F traces upon electric shock (black dotted line). Right: Average traces (black) of calcium events (grey) after electric shock. (n = 8 larvae, 16 events). Scale bar = 20 μm.

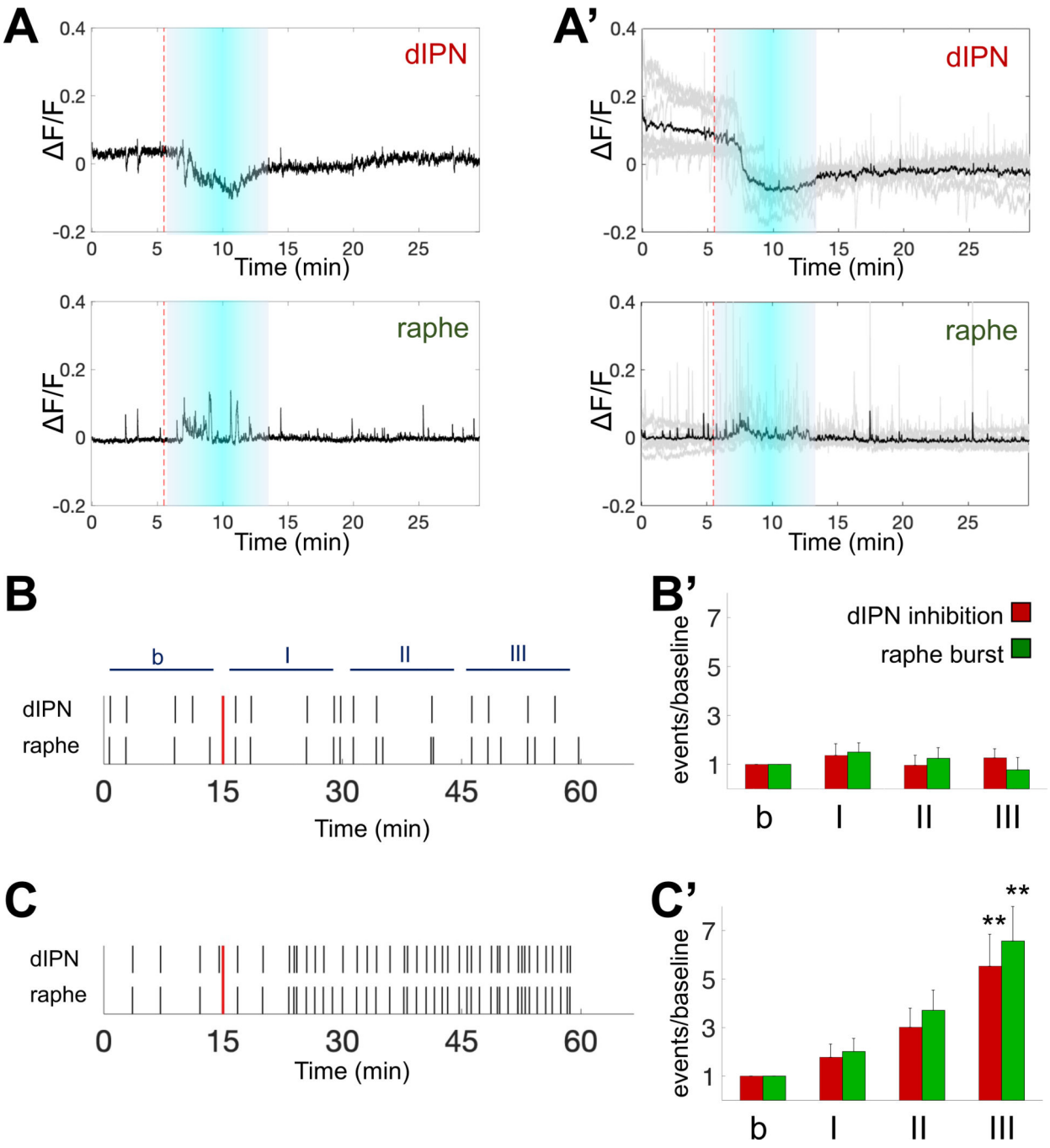

Figure 3. Nicotine induces prolonged negatively correlated event

(A) Representative ΔF/F traces from dHb terminals in *Tg(gng8:GAL4ff)*^{c426}*;Tg(UAS:GCaMP7a*) explant. 5 min nicotine (10 μM) perfusion induces inhibition at the dIPN (top) and bursts at the raphe (bottom).

(A') Average ΔF/F traces (black) of nicotine-induced negatively correlated events (grey). Duration (cyan boxes) and initiation (red dotted lines) of nicotine application indicated. n = 8 explants.

(B,C) Representative raster plots of dIPN inhibition and raphe burst events. (B) Control and (C) nAChR antagonist (100 μM mecamylamine and 10 μM d-tubocurarine) application. Introduction of E3 solution (B) or antagonists (C) indicated (red lines).
(B',C') Ratio of average number of events in 15-minute windows (I, II, III) and baseline activity (b) after applying (B') E3 (n = 4) or (C') antagonists (n = 6). Bars indicate negatively correlated events in dHb terminals at the raphe (green, bursts) and dIPN (red, inhibition). One-way ANOVA followed by Tukey's test, ** $p<0.005$. b: 15 minutes of baseline, I: 0–15, II: 15–30, III: 30–45 min after application.

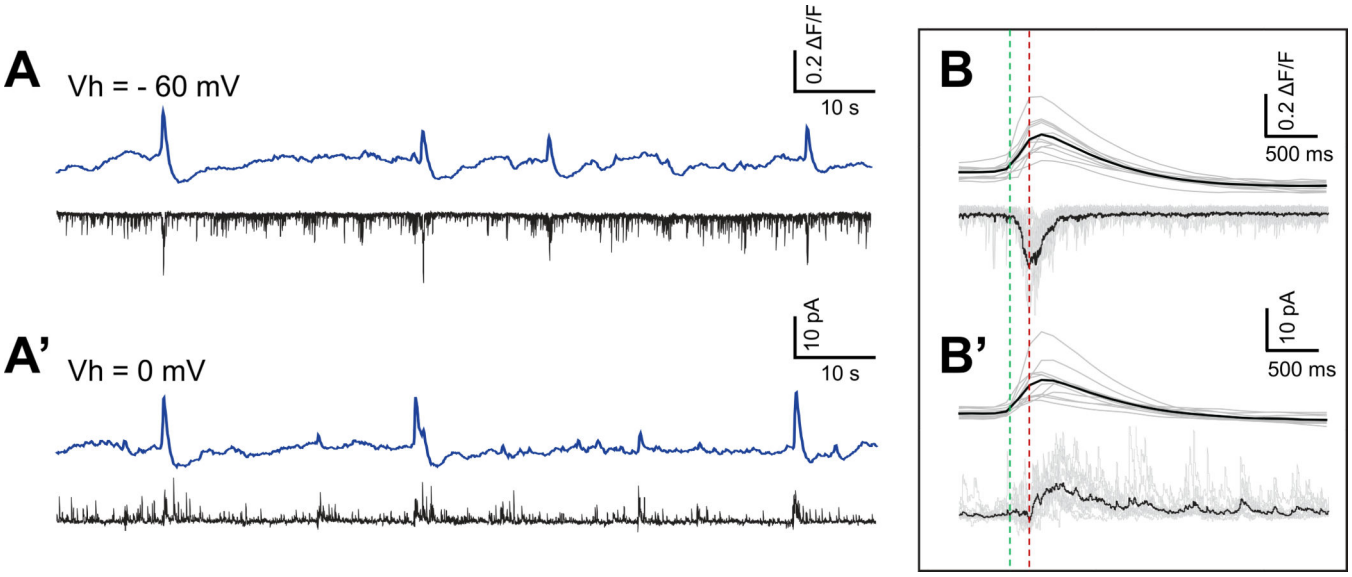

Figure 4. Calcium bursts correspond to acetylcholine/glutamate and GABAergic currents

(A-A') ΔF/F traces of dHb terminals (blue) aligned with simultaneous patch-clamp recording of IPN neurons (black) show correlation of calcium bursts with increase in glutamatergic/cholinergic inward currents (A, Vh = −60 mV) and GABAergic outward currents (A', Vh = 0 mV).

(B-B') Average traces (black) of calcium bursts (top) aligned with synaptic responses (bottom) at holding potentials of –60 mV (B, n = 4 explants, 42 events) and 0 mV (B', n = 3 explants, 23 events). Dotted lines indicate onset for inward (green) and outward (red) currents.

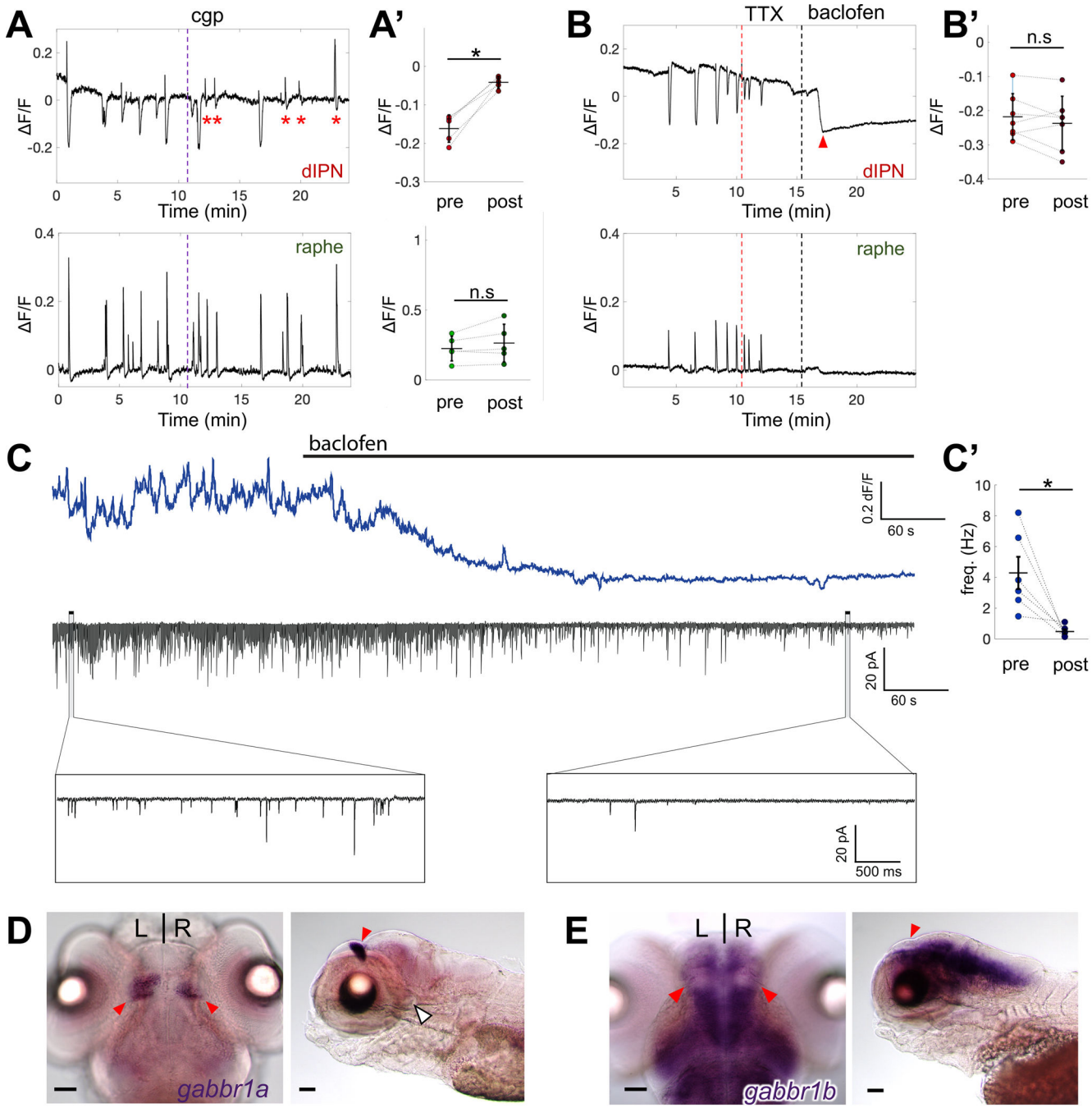

Figure 5. Calcium inhibition occurs via presynaptic $GABA_B$ receptors

(A-B) Representative ΔF/F traces in terminals at dIPN (top) and raphe (bottom) after application of (A) 1 μM cgp55845 or (B) 3 μM tetrodotoxin (TTX) + 2 μM baclofen. Time of drug application indicated (vertical lines).

(A') Average peak amplitude before and after cgp55845 application in terminals at the dIPN (−0.16 ± 0.03 vs −0.04 ± 0.01) and raphe (0.22 ± 0.09 vs. 0.26 ± 0.13) during inhibition (top) and burst (bottom). n = 6 explants, 50 events. Red asterisks indicate attenuated calcium inhibition at the dIPN after cgp55845 application.

(B') Paired plots comparing average inhibition amplitude in control conditions (−0.22 ± 0.07) to the average baseline decrease after baclofen application (−0.24 ± 0.08). n = 7 explants, 46 events. Note abrupt decrease (red arrowhead) in baseline at the dIPN following baclofen.

(C) ΔF/F traces of IPN (top) aligned with simultaneous whole-cell patch-clamp recording trace (middle) upon baclofen perfusion. Time of baclofen application indicated (black bar). Magnified traces of synaptic activity before (left) and after (right) baclofen (bottom panels).

(C') Paired plot of synaptic activity frequency before (4.29 ± 1.05 Hz) and after (0.47 ± 0.15 Hz) baclofen. n = 6 explants. Mean ± SD indicated in (A', B', C').

(D,E) Dorsal (left) and sagittal (right) views of *gabbr1a* (D) and *gabbr1b* (E) expression at 6 dpf. dHb nuclei (red arrowheads) and absence of expression at IPN (white arrowhead) (D). Wilcoxon signed-rank test. * $p < 0.05$. Scale bars: 50 μm.

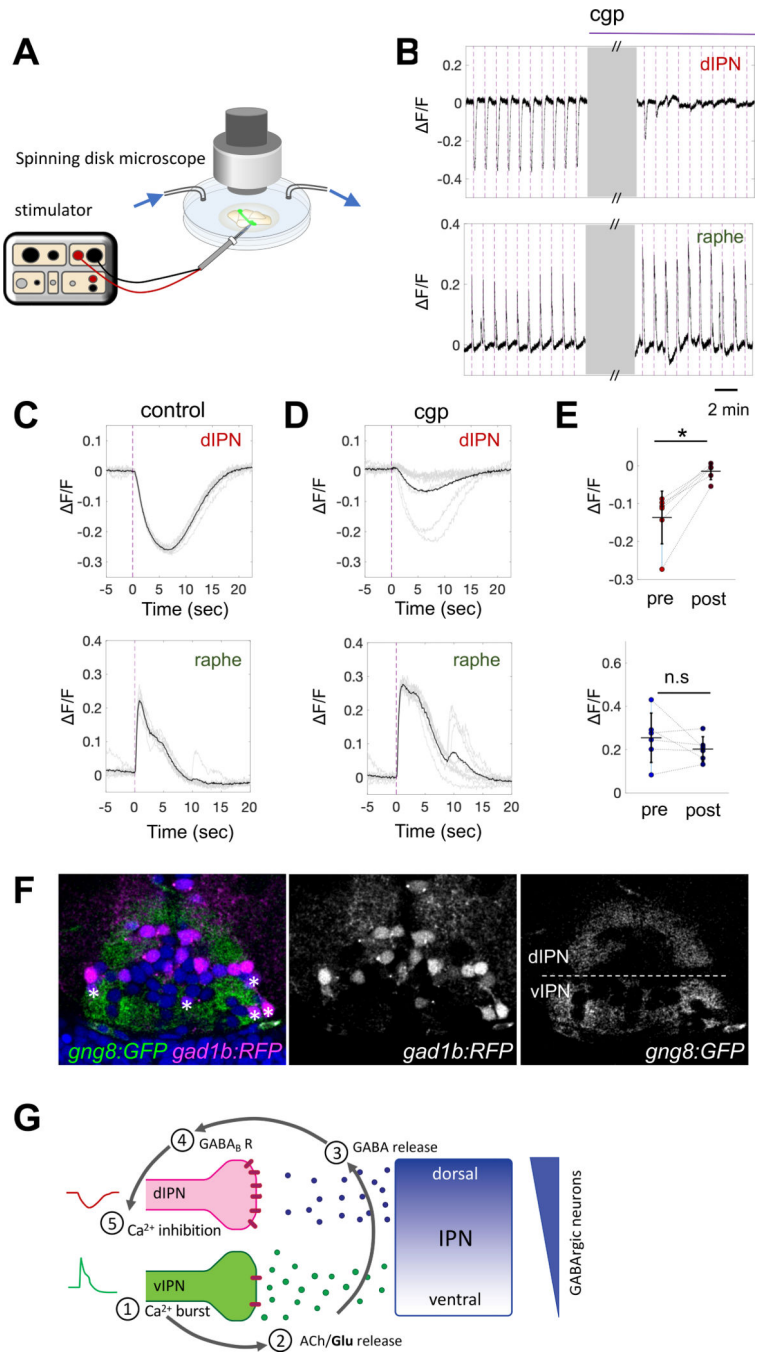

Figure 6. Direct stimulation of IPN induces GABA$_B$ receptor-mediated inhibition in terminals at the dIPN

(A) Schematic of setup for simultaneous electrical stimulation and drug perfusion.

(B) Representative ΔF/F traces showing attenuation of dIPN inhibition by electrical stimulation after cgp55845 perfusion (top), with bursts unaffected in the raphe (bottom). Grey boxes represent 10 min after cgp55845 application. See also Video S4.

(C,D) Average traces (black) of calcium events (grey, 10 stimuli) before (c) and after (d) cgp55845.

(E) Paired plot of average peak amplitudes before and after cgp55845 application during inhibition (top, −0.15 ± 0.07 vs. −0.02 ± 0.02) and burst (bottom, 0.22 ± 0.08 vs 0.2 ± 0.06). n = 6 explants, 71 events. Purple dotted lines indicate time of electrical stimulation (B-D). Purple line in (B) denotes duration of cgp55845 application. Wilcoxon signed-rank test, * p< 0.05, n.s. not significant. Mean ± SD indicated.

(F) Transverse section of *Tg(gng8:GAL4ff)*^{c426}*;Tg(UAS:GFP)*^{c426}*;Tg(gad1b:|R|-GFP)* larval IPN surrounded by dHb terminals (green) and GABAergic neurons (magenta). Hoechst nuclear staining (blue). White asterisks indicate gad1b:RFP^{+} neurons in vIPN. White dotted line separates dIPN and vIPN (right panel).

(G) Model illustrating the mechanism underlying negatively correlated events in dHb terminals at the IPN (see discussion).

KEY RESOURCES TABLE

REAGENT or RESOURCE	SOURCE	IDENTIFIER
Antibodies		
rabbit anti-VAChT	Synaptic Systems	Cat# 139103; RRID:AB_887864
Bacterial and virus strains		
Subcloning Efficiency™ DH5α Competent Cells	Life Technologies	Cat# 18265017
Biological samples		
Chemicals, peptides, and recombinant proteins		
Tricaine	Sigma-Aldrich	Cat# A5040-25
Mecamylamine hydrochloride	Tocris Biosciences	Cat# 2843
(+)-D-tubocurarine chloride	Tocris Biosciences	Cat# 2820
Nicotine ditartrate	Acros Organics	Cat# N0590200
Tetrodotoxin	Tocris Biosciences	Cat# 1069
Baclofen	Tocris Biosciences	Cat# 0796
Cgp55845	Tocris Biosciences	Cat# 1248
Hoechst 33342	Life Technologies	Cat# H3570
Mowiol 4-88	Sigma-Aldrich	Cat# 475904
Pancuranium bromide	Sigma-Aldrich	Cat# P1918
NaCl	Sigma-Aldrich	Cat# S7653
KCl	Sigma-Aldrich	Cat# P9333
$MgCl_2$	VWR/Avantor	Cat# 12315.A1
HEPES	Sigma-Aldrich	Cat# H4034
Glucose	Sigma-Aldrich	Cat# G6152
$CaCl_2$	Sigma-Aldrich	Cat# C8106
Low melting agarose	Life Technologies	Cat# R0801
PFA	EMS	Cat# 15710
Glycerol	Sigma-Aldrich	Cat# G6279
T7 polymerase	NEB	Cat# M0251S
KpnI HF	NEB	Cat# R3142S
Critical commercial assays		
TOPO®TA cloning Kit	Life Technologies	Cat# 450640
Platinum™ *Taq* DNA Polymerase High Fidelity	Life Technologies	Cat# 11304011
Deposited data		
Experimental models: Cell lines		
Experimental models: Organisms/strains		
TgBAC(gng8:GAL4ff)^{c426}	[9]	Zfin : ZDB-ALT-140423-2
Tg(UAS:GCaMP7a)	[42]	Zfin : ZDB-TGCONSTRCT-131030-2.
Tg(UAS:GFP)^{c354}	[43]	ZDB-TGCONSTRCT-131029-7
Tg(gad1b:|R|-GFP)	[20]	ZDB-ALT-131127-6

REAGENT or RESOURCE	SOURCE	IDENTIFIER
Tg(nptx2:Gal4-VP16)^{rw0143a}	[5]	ZDB-ALT-110215-5
Oligonucleotides		
Primer : gabbr1a Reverse	[19]	
Primer : gabbr1b Reverse	[19]	
Primer : gabbr1a Forward - ACGTATGGTTCCTCATCGGC	This paper	N/A
Primer : gabbr1b Forward – AGACAAGAGAAAGCACCTGGA	This paper	N/A
Recombinant DNA		
Software and algorithms		
Fiji	FIJI	http://fiji.sc RRID:SCR_002285
MATLAB	Mathworks	http://www.mathworks.com/products/matlab/ RRID:SCR_001622
pClamp	Molecular Devices	http://www.moleculardevices.com/products/software/pclamp.html RRID:SCR_011323
Clampfit 10	Molecular Devices	http://www.moleculardevices.com/products/software/pclamp.html
HCImage Live software	Hamamatsu, Japan	https://hcimage.com/
ImageJ Mosaic Plug-ins	National Institute of Health, USA	http://ncmir.ucsd.edu/downloads/montaging_plugins.shtm RRID:SCR_001935
MetaMorph Microscopy Automation and Image Analysis Software	Molecular Devices	http://www.moleculardevices.com/Products/Software/Meta-Imaging-Series/MetaMorph.html RRID:SCR_002368
GraphPad Prism	Molecular Devices	http://www.moleculardevices.com/products/software/pclamp.html
R Project for Statistical Computing	R	http://www.r-project.org/ RRID:SCR_001905
Other		
Perfusion peristaltic pump	Ismatec	http://www.ismatec.com/int_e/pumps/g_gearpumps/gearpumps.htm
Spinning Disc Microscope - Axio Examiner.Z1	Zeiss	https://www.zeiss.com/microscopy/int/products/light-microscopes/axio-examiner-for-biology.html
SP5 laser scanning confocal microscope	Leica	https://www.leica-microsystems.com/fr/produits/microscopes-confocaux/informations-detaillees/leica-tcs-sp5/
Epifluorescence Microscope BX51W1	Olympus	https://www.olympus-lifescience.com/en/microscopes/upright/bx61wi/
Multiclamp 700B amplifier	Molecular Devices	https://www.moleculardevices.com/products/axon-patch-clamp-system/amplifiers/axon-instruments-patch-clamp-amplifiers
Digidata 1440 acquistion system	Molecular Devices	https://www.moleculardevices.com/sites/default/files/en/assets/user-guide/dd/cns/digidata-1440a-low-noise-data-acquisition-system.pdf
Orca Flash4.0	Hamamatsu, Japan	https://www.hamamatsu.com/eu/en/product/type/C13440-20CU/index.html
Orca 03G	Hamamatsu, Japan	http://www.hamamatsu.com.cn/UserFiles/DownFile/Product/20130929214608556.pdf
Vibratome VT1000 S	Leica	https://www.leicabiosystems.com/histology-equipment/sliding-and-vibrating-blade-microtomes/vibrating-blade-microtomes/leica-vt1000-s/

REAGENT or RESOURCE	SOURCE	IDENTIFIER
Nikon Eclipse E800 microscope.	Nikon	https://www.microscopyu.com/museum/eclipse-e800
DS3 isolated constant current stimulator	Digitimer, Ltd.	uct/life-science-research/stimulators/ds3-isolated-current-stimulator/
Master-8 pulse generator	A.M.PI	http://www.ampi.co.il/
Thermocycleur Doppio Gradient	VWR/Avantor	Cat# 732-2552